Supplementary information: Exciton-polariton condensate in the van der Waals magnet CrSBr

Bo Han[1,7], Hangyong Shan[1,7], Kok Wee Song[2], Lukas Lackner[1], Martin Esmann[1], Vita Solovyeva[1], Falk Eilenberger[3,4,5], Jakub Regner[6], Zdeněk Sofer[6], Oleksandr Kyriienko[2] and Christian Schneider[1,*]

[1] *Institute of Physics, Faculty V, Carl von Ossietzky University Oldenburg, 26129 Oldenburg, Germany.*
[2] *Department of Physics and Astronomy, University of Exeter, Exeter EX4 4QL, United Kingdom.*
[3] *Institute of Applied Physics, Abbe Center of Photonics, Friedrich Schiller Universität Jena, 07745 Jena, Germany.*
[4] *Fraunhofer-Institute for Applied Optics and Precision Engineering IOF, 07745 Jena, Germany.*
[5] *Max Planck School of Photonics, 07745 Jena, Germany.*
[6] *Department of Inorganic Chemistry, Faculty of Chemical Technology, University of Chemistry and Technology Prague, Technická 5, Prague 6, 16628, Czech Republic.*
[7] *These authors contributed equally.*
* *E-mail: christian.schneider@uni-oldenburg.de*

Contents

Supplementary note 1: Further details of sample and cavity structures

Polarization-resolved measurements. The polarizers on the excitation and detection are aligned to the crystallographic b-axis by searching for the maximum PL emission intensity. A half waveplate on the detection side rotates the polarization of the signal to realize the polarization-resolved measurements. Supplementary Fig. 1f shows that the PL emission of a LPB mode of CrSBr in the external cavity is linearly polarized along the crystal b-axis. The fit yields a unity polarization degree along the crystallographic b-axis.

Cavity Q-factor. Figure. S1e contains the reflection of an empty cavity with a gap of 4025 nm, which is simulated by the transfer matrix method. For this geometry, two sharp cavity modes present in the energy range of the self-hybridized polaritons. The mode at 1.353 eV has a Q-factor of 5700, while the other mode at 1.249 eV has a Q-factor of 8600. Although the simulated quality factor (Q-factor) by the transfer matrix methods for our symmetrical dielectric cavity structure is above 5000, the measured Q-factor$\sim$1100 of the transverse modes is substantially smaller than the simulated result. The discrepancy is caused by the vibration of the cavity length, which is in a same frequency $\sim$1.4 Hz as the closed-cycle helium pulses. As a result, the cavity resonance is broadened up to $\sim$1.1 meV (see Figs. 2d,g of the manuscript). We note that the considerably compromised Q-factor is still much larger than the Q-factors of cavity structures in previous works (Q-factor$\sim$300) using the hybrid of metallic and dielectric mirrors[1,2]. It also does not impede us from the strong light-matter coupling regime and the exciton-polariton condensate.

Supplementary note 2: Optical properties of sample position 1 and 2

Figure 1d of the manuscript presents the cavity detuning PL on sample position 1. Fig. S4a-c present the cavity detuning PL on sample position 2 in different magnetic orders. The measurements on position 2 are performed with 0.5 mW pulsed laser (725 nm, 200 fs pulse width and 76 MHz repetition rate) at cryogenic temperature of 3.5 K. At 0 T, sample position 2 also exhibits six self-hybridized polariton states (P_1-P_6) as position 1. The energies of the self-hybridized polaritons used in the fitting and the coupling strengths are all summarized in Table. S1. We note that the experimentally extracted coupling strengths of the self-hybridized polaritons are nearly constant in both magnetic orders.

	P_1	P_2	P_3	P_4	P_5	P_6	V_1	V_2	V_3	V_4	V_5	V_6
Pos. 1 (AFM)	1.3604	1.3578	1.3540	1.3480	1.3341	1.2895	3.0	4.6	5.6	8.0	15.4	33.0
Pos. 2 (AFM)	1.3660	1.3634	1.3597	1.3540	1.3395	1.2944	4.0	5.0	5.6	9.0	16.4	37.4
Pos. 2 (FM)	1.3515	1.3482	1.3442	1.3376	1.3248	1.2827	4.6	4.6	5.2	9.0	16.4	36.0

Supplementary Table. S1| Self-hybridized polariton energies and coupling strengths. The polaritonic energies (P_1-P_6) are in unit of eV, while the coupling strengths (V_1-V_6) are in unit of meV.

Supplementary note 3: Polariton non-linearity measurements

Polaritonic non-linearities with different cavity detunings and magnetic orders are obtained via PL measurements on sample position 2. For each power dependent study, we keep the cavity detuning (voltage) constant between 32-52 V as in Fig. S4a for the AFM order (0 T) and 22-46 V as in Fig. S4b for the FM order (3 T). The experimental results are compiled in Fig. S3. The energy shifts of the lowest LPBs are then fitted and summarized in Figs. S4d,e.

For all detuning cases in the AFM order, the LPB firstly experience a moderate linear redshift, and then a giant blueshift follows until the condensate depletes. However, for the detuning cases in the FM order, the energy slope of LPB at low pump powers changes sign from moderate redshift to moderate blueshift, as the detuning voltage is tuned above 36 V in Fig. S4b. And at high pump powers, the giant blueshift in FM order is similar to that in AFM order. By using a linear fit of the LPB energy shifts below 20 mW, the energy slopes (empty spherical symbols) for different detuning scenarios and magnetic orders are obtained and summarized in Fig. S4j.

We can see that the energy shifts in low power range of the LPB in AFM and FM orders present obviously opposite trends. As the LPB becomes more excitonic (at higher DC voltages), the redshift slope of the LPB in the AFM order becomes smaller (larger amplitude), while in the FM order the slope keeps increasing. This magnetic order dependent phenomena have been observed for the magnetic excitons in CrSBr as a result of coupling to the incoherent magnons that are excited by the temperature[1]. In addition, we note that the redshift should not exists for the highly photonic LPB (22 V) in the FM order because of the much reduced excitonic components and correspondingly little interaction between excitons and incoherent magnons. This effect is actually caused by the redshift of the cavity modes due to the thermal expansion of our open cavity as pump power ramps up. Another proof of cavity thermal expansion is that the extrapolation of the slope value in the AFM order towards the pure photonic regime converges with the FM scenario around -0.05 meV/mW, which is supposed to be the pure contribution from the cavity thermal drift.

To quantify the redshift due to the cavity drift, we need to know the photonic Hopfield coefficients that are specifically contributed by the external cavity modes. Figs. S4h,i show the Hopfield coefficients of the LPB mode in AFM and FM orders, respectively, which are calculated by using a 2×2 coupled oscillator model that considers only the P_6 self-hybridized polariton mode and the C_2 cavity mode:

$$\begin{pmatrix} E_{c_2} & V_6/2 \\ V_6/2 & E_{P_6} \end{pmatrix} \tag{1}$$

$$E_{\mathrm{LPB}} = \frac{1}{2}[E_{c_2} + E_{P_6} - \sqrt{V_6^2 + (E_{c_2} - E_{P_6})^2}] \tag{2}$$

$$|P_6|^2 = \frac{1}{2} + \frac{E_{c_2} - E_{P_6}}{2\sqrt{(E_{c_2} - E_{P_6})^2 + V^2}} \tag{3}$$

$$|C_2|^2 = \frac{1}{2} - \frac{E_{c_2} - E_{P_6}}{2\sqrt{(E_{c_2} - E_{P_6})^2 + V^2}} \tag{4}$$

This model is valid for two reasons. Firstly, the energy difference between P_5 and P_6 intrinsic polaritonic modes is larger than the coupling strength V_6, so that the strong coupling of P_6 to the external cavity modes can be regarded as independent of other self-hybridized polariton resonances (P_1-P_5). Secondly, the usage of two additional cavity modes in our 9×9 coupled oscillator model in Figs. S4a,b only becomes vital for unconventional polariton dispersion in either highly photonic (∼5 V) or highly excitonic (∼60 V) cases, so that utilizing only the middle cavity mode 'c_2' has negligible influence to the detunings where the polaritonic non-linearities (Fig. S3) are measured.

We note that the Hopfield coefficients in Figs. S4h,i only represent the proportionalities of P_6 self-hybridized polariton and the external cavity mode in the LPB. The excitonic and total photonic Hopfield coefficients should be renormalized by taking into account the intrinsic self-hybridization in our CrSBr flake. For example, using the methods provided in a previous work[1], the excitonic Hopfield coefficient of P_6 mode with a total magnetic shift of -13.3 meV (left panel of Fig. 1e in the manuscript), is determined as $|X|^2_{P_6}$= 0.76. In presence of an external cavity, the excitonic admixture will be further diluted. For the lowest LPBs in Fig. S4c (44 V, 0 T and 38 V, 3 T on position 2), the Hopfield coefficient of P_6 self-hybridized polariton is $|P_6|^2$= 0.74, which means the LPB has an excitonic Hopfield coefficient $|X|^2$=$|X|^2_{P_6} \times |P_6|^2$= 0.56 and total photonic Hopfield coefficient $|C|^2$= 0.44. These results are consistent with the $|X|^2$= 0.49 and $|C|^2$= 0.51 of the lowest LPB in a similar cavity detuning scenario (36 V) on sample position 1 (see Fig. S2), which is directly calculated by using its magnetic shift.

In the following, we calibrate the polariton non-linearity by removing the contribution from cavity redshifts with increasing pump power. We use the experimentally extracted redshift slope $s = -0.0474$ meV/mW of the LPB mode at 22 V cavity detuning ($|C_2|^2$=0.907) of the FM order to calculate the pure cavity drift slope due to the thermal expansion: $s_0 = \frac{s}{|C_2|^2}$=-0.0523 meV/mW. We then use s_0 to renormalize the cavity redshift slope of each detuning by multiplying their photonic Hopfield coefficients $|C_2|^2$. We obtain the redshift caused by the cavity thermal expansion $\delta = s_0 P$, where P is the pump power. The LPB mode energy modified by the cavity drift is

$$E'_{\mathrm{LPB}} = \frac{1}{2}[E_{c_2} + E_{P_6} + \delta - \sqrt{V_6^2 + (E_{c_2} + \delta - E_{P_6})^2}]. \tag{5}$$

The polariton redshift caused by the cavity expansion is then

$$\Delta = E'_{\mathrm{LPB}} - E_{\mathrm{LPB}} = \frac{1}{2}[\delta - \sqrt{V_6^2 + (E_{c_2} + \delta - E_{P_6})^2} + \sqrt{V_6^2 + (E_{c_2} - E_{P_6})^2}]. \tag{6}$$

The experimental values of the polariton non-linearity in Figs. S4d,e are then corrected by removing an offset of Δ, the results of which are presented in Figs. S4f,g. The slopes below 20 mW of the corrected data are fitted and plotted as the filled spherical symbols in Fig. S4j. Now, we see that the extrapolation of the corrected slopes in the AFM order towards highly photonic regime converges with the corrected slopes in the FM scenario at 0 meV/mW. For more excitonic regimes that are DC voltages >40 V in FM order and >44 V in AFM order, the compensation effect of cavity drift is nearly negligible. In low power regime, the LPB redshifts (blueshifts) in AFM (FM) order for all cavity detunings. In high power regime, the LPB has giant blueshifts for both magnetic orders and all cavity detuning scenarios.

Supplementary note 4: Exciton density estimation

The pump is a λ = 725 nm laser that has a 200 fs pulse duration at a pulse-repetition frequency (PRF) of 76 MHz. The energy of a single pulse with P=1 mW measured average power is

$$E_{\mathrm{pulse}}^{1mW} = \frac{P}{PRF} = \frac{10^{-3}\ W}{76 \times 10^6\ Hz} \simeq 1.316 \times 10^{-11}\ J = 13.16\ pJ. \tag{7}$$

The energy of one photon is

$$E_{\mathrm{photon}} = \frac{hc}{\lambda} \simeq 2.74 \times 10^{-19} J = 2.74 \times 10^{-7} pJ, \tag{8}$$

where $h = 6.62607015 \times 10^{-34} J$ Hz^{-1} and $c = 2.99792458 \times 10^8\ m$ Hz are the Planck constant and vacuum light speed, respectively. The number of photons in a single pulse with average powers of 1 mW and 50 mW are

$$\begin{aligned} n_{\mathrm{photon}}^{1mW} &= \frac{E_{\mathrm{pulse}}^{1mW}}{E_{\mathrm{photon}}} = 4.80 \times 10^7, \\ n_{\mathrm{photon}}^{50mW} &= 2.40 \times 10^9. \end{aligned} \tag{9}$$

We utilize transfer matrix methods to simulate the open cavity structure (DBR/gap/CrSBr/DBR). Applying a cavity gap of 4025 nm yields polariton modes matching very well the PL spectrum in the AFM order and 44 V cavity detuning (Fig. S5a). The electric field intensity of 725 nm incidence is normalized for the simulations. Its amplitude drops to 0.009 in the CrSBr slab and 0.03 in the bottom DBR, signifying much stronger dielectric property of the CrSBr than the materials consisting of DBR (Fig. S5b). We subsequently quantify the absorption of the cavity system at 725 nm: A=1-R-T=0.0209 (Fig. S5a). The exciton number for a 50 mW average excitation power is thus calculated as

$$n_X^{50mW} = A \cdot n_{\mathrm{photon}}^{50mW} \simeq 5.02 \times 10^7. \tag{10}$$

We exclude the excitation scenarios by more than one laser pulses. The exciton reservoir depletes completely before the arrival of a following laser pulse because the exciton lifetime $\sim$15 ps[3] in a CrSBr flake with similar thickness of 400 nm is three orders shorter than the pulse interval of 13.16 ns in our experiments. The polariton lifetime is supposed to be even shorter than the pure exciton scenario. Considering a layer thickness of 0.8 nm[4,5], our 312 nm CrSBr flake contains $m = 390$ layers. The excitation area on CrSBr S_X=$\pi \cdot r^2$=$9\pi\mu$m^2 is referred from the burned regions in Fig. S1c. For an average pump power of 50 mW, the exciton density in each CrSBr layer is thus derived as

$$d_X^{50mW} = \frac{n_X^{50mW}}{m \cdot S_X} \simeq 4.53 \times 10^3 \mu m^{-2} = 4.54 \times 10^{11} cm^{-2} \tag{11}$$

Based on Eq. (11), we can rescale the exciton density of each layer for other pump powers (Fig. S5c). We can see that for this maximum pump power applied in our experiments, the exciton density in each CrSBr layer is well below the Mott density $n_{\mathrm{Mott}} \sim 10^{13}\mathrm{cm}^{-2}$ in the transition metal dichalcogenide monolayers[6,7]. It is comparable to $n_{\mathrm{Mott}} \sim 10^{11}\mathrm{cm}^{-2}$ in III-V[8–10] and II-VI[11,12] semiconductor quantum wells. However, due to the highly anisotropic reduced masses and dielectric properties, the excitonic wavefunction is quasi-1D along the b-axis with substantial charge density on the orbitals of Chromium and Sulfur[13–16]. The exciton radii along the a-axis[13,17] are on the same order of the unit cell scales[16,18], so that the excitons in CrSBr can be regarded as mixed Frenkel and Wannier-Mott type[13,17]. This is in analogy to the single-wall carbon nanotubes where the excitons are 1D along the tube axis, and show both the Frenkel and Wannier-Mott characteristics[19–22]. The 1D confinement in hexagonal Boron Nitride (hBN) nanotubes also leads to Frenkel excitons[23,24] that can be distinguished from the Wannier-Mott excitons in the flat hBN[25]. In general, owing to the smaller exciton size, the Mott density of Frenkel excitons is supposed to be higher than their Wannier-Mott counterparts.

To be more quantitative, the effective exciton Bohr radius in CrSBr ($a_B \sim 1.2$ nm)[17] is considerably smaller than those Wannier-Mott excitons ($a_B \geq 4$ nm) in conventional III-V and II-VI semiconductor systems[26], so that in a rough estimation[27] the Mott density $\mathrm{n_{Mott}} \sim \mathrm{a}_B^{-2}$ in CrSBr ought to be at least one order of magnitude higher than the 10^{11} order. Therefore, We suppose that during the whole polariton nonlinearity measurements our system should not have experienced Mott transition where the electrons and holes are in a weak Coulomb-correlated plasma instead of the bound excitonic states[28,29].

Supplementary note 5: Theoretical model for exciton-magnon coupling

Exciton Here, we describe a theoretical model for excitons in CrSBr samples. We consider a system with bilayer configuration, as this allows to understand the overall behaviour in the presence of interlayer hybridization and spin ordering. The excitonic energy can be written as

$$E_X(\theta_1, \theta_2) = \varepsilon_g(\theta_1 - \theta_2) + E_b + \rho_{\mathrm{X}} g_{\mathrm{X}}, \tag{12}$$

where E_b is the exciton binding energy, and ε_g is the energy bandgap that accounts for corrections from magnetic ordering. This is described by angles θ_1 and θ_2 between the external magnetic field and the spin in layer 1 (upper) and and layer 2 (lower). The bandgap of the material can be described as

$$\varepsilon_g(\theta_1 - \theta_2) = \varepsilon_0 + t \cos\left(\frac{\theta_1 - \theta_2}{2}\right), \tag{13}$$

including the dependence on the relative spin direction of the spin in upper and lower layer. This spin-dependent term originates from an overlap between interlayer spin wavefunctions. The overlap amplitude t is estimated to be 12 meV from our experiment (Fig. 1e). In the presence of background exciton with density ρ_{X}, this will lead to the non-linear shift of the exciton due to exciton-exciton exchange interaction.

To theoretically estimate g_{X}, we first model the exciton by the following creation field operator as

$$X_\sigma^\dagger = \sum_{\ell_c \ell_v} \sum_{\mathbf{k}} C^\sigma_{\ell_c \ell_v} \psi_\sigma^{\ell_c \ell_v}(\mathbf{k}) a^\dagger_{\ell_c \mathbf{k} \sigma} b_{\ell_v, -\mathbf{k}\sigma}, \tag{14}$$

where $\psi_\sigma^{\ell_c \ell_v}(\mathbf{k})$ is the exciton wavefunction with σ and $\mathbf{k}$ being the spin and in-plane crystal momentum. The layer index for conduction band electron is ℓ_c and for valence band hole ℓ_v. As previously mentioned, we model our system by a bilayer CrSBr ($\ell_c, \ell_v = 1, 2$), as this is the minimal case to investigate interlayer-intralayer hybridization effects. We note that including more layers into the theory will not change the result qualitatively.[30] With this, the intralayer exciton wavefunction are $\psi_\sigma^{11}(\mathbf{k})$, $\psi_\sigma^{22}(\mathbf{k})$ and the interlayer wavefunctions are $\psi_\sigma^{12}(\mathbf{k})$, $\psi_\sigma^{21}(\mathbf{k})$. The interlayer and intralayer exciton hybridization coefficient is $C_\sigma^{\ell\ell'}$. The creation field operator of conduction band and the annihilation field operator of the valance band is $a_{\mathbf{k}\sigma}^\dagger$ and $b_{\mathbf{k}\sigma}$.

The intralayer and interlayer excitonic states satisfy the Wannier equation

$$[\varepsilon_c(\mathbf{k}) - \varepsilon_v(\mathbf{k})]\psi_\sigma^{\ell_c\ell_v}(\mathbf{k}) - \sum_{\mathbf{q}} w_{\ell_c\ell_v}(\mathbf{q})\psi_\sigma(\mathbf{k}+\mathbf{q}) = E_\sigma^{\ell_c\ell_v}\psi(\mathbf{k}), \tag{15}$$

where we adopted the Keldysh-like potential in the CrSBr bilayer. We consider the mass anisotropies in the dispersion

$$\varepsilon_c(\mathbf{k}) = \frac{k_x^2}{2m_{cx}} + \frac{k_y^2}{2m_{cy}}, \quad \varepsilon_v(\mathbf{k}) = -\frac{k_x^2}{2m_{vx}} - \frac{k_y^2}{2m_{vy}}. \tag{16}$$

The conduction band masses are $m_{cx} = 7.31m_0$, $m_{cy} = 0.14m_0$ and the valence band mass are $m_{vx} = 2.84m_0$, $m_{vy} = 0.45m_0$[13].

In CrSBr bilayer, we model the screened Coulomb interaction as[31]

$$v_{\ell\ell'}(\mathbf{q}) = \frac{2\pi}{\epsilon q}\frac{\kappa_{\ell\ell'}(q)}{(1+r_*q)^2 - r_*^2q^2\mathrm{e}^{-2qd}}, \tag{17}$$

where $d = 7.93$Å[32] is the interlayer distance of the bilayer CrSBr $\kappa_{12}(q) = \kappa_{21}(q) = \mathrm{e}^{-qd}$ and $\kappa_{11}(q) = \kappa_{22}(q) = 1 + r_*q(1-\mathrm{e}^{-2qd})$. The screening length is[30,33–35]

$$r_* = \frac{\epsilon_s - 1}{\epsilon}d, \tag{18}$$

where ϵ is the dielectric constant of the environment and ϵ_s is the dielectric constant of CrSBr. Here, we let $\epsilon_s \sim 6$ which gives binding energy $E_\sigma^{11} = E_\sigma^{22} \approx 537$ meV in vacuum ($\epsilon = 1$). In this calculation, we ignore the anisotropic screening for simplicity.

In anti-ferromagnetic (AFM) phase, interlayer tunneling is not allowed. However, in the ferromagnetic (FM) phase, the intralayer and interlayer excitons hybridized due to interlayer electrons tunneling. To account for the hybridization, we can solve for the coefficients $C_\sigma^{\ell\ell'}$[36] as

$$\begin{bmatrix} E_\sigma^{11} & -T_v & T_c & 0 \\ -T_v^* & E_\sigma^{12} & 0 & T_c \\ T_c^* & 0 & E_\sigma^{21} & -T_v \\ 0 & T_c^* & -T_v^* & E_\sigma^{22} \end{bmatrix} \begin{bmatrix} C_\sigma^{11} \\ C_\sigma^{12} \\ C_\sigma^{21} \\ C_\sigma^{22} \end{bmatrix} = E_b \begin{bmatrix} C_\sigma^{11} \\ C_\sigma^{12} \\ C_\sigma^{21} \\ C_\sigma^{22} \end{bmatrix}, \tag{19}$$

where the transition matrix elements are

$$T_v = t_v \sum_{\mathbf{k}} \bar{\psi}_\sigma^{11}(\mathbf{k})\psi_\sigma^{12}(\mathbf{k}), \quad T_c = t_c \sum_{\mathbf{k}} \bar{\psi}_\sigma^{11}(\mathbf{k})\psi_\sigma^{12}(\mathbf{k}). \tag{20}$$

Here, we consider the relevant valence band interlayer hopping $t_v = t = 12$ meV and $t_c = 0$.[13]

In our analysis, we concentrate on $1s$ states and set the total momentum of the exciton be $\mathbf{Q} = 0$ in the scattering processes, such that we characterize the low-energy exciton-exciton (X-X) interactions with elastic scattering for $\mathbf{Q} = 0$ only. The X-X interaction between exciton can be calculated from the total energy of the two-exciton state,

$\Omega_\sigma = \langle 0|X_\sigma X_\sigma \mathcal{H} X^\dagger_\sigma X^\dagger_\sigma|0\rangle = 2E_b + \Delta_\sigma$. The interacting potential energy is given by

$$\Delta_\sigma = -2\sum_{ss'}\sum_{\tilde{s}\tilde{s}'}\bar{C}^\sigma_{s'}\bar{C}^\sigma_{\tilde{s}'}C^\sigma_s C^\sigma_{\tilde{s}} V^{s'\tilde{s}'}_{s\tilde{s}}, \tag{21}$$

where $s = (\ell_c, \ell_v)$ is the layer double index. The exchange interaction reads

$$V^{s'\tilde{s}'}_{s\tilde{s}} = \frac{1}{2A}\sum_{\mathbf{k}\tilde{\mathbf{k}}\mathbf{q}}\sum_{\ell\ell'} f^{\ell}_{s\sigma}(\mathbf{k},\mathbf{q}) w_{\ell\ell'}(\mathbf{q}) f^{\ell'}_{\tilde{s}\sigma}(\mathbf{k},-\mathbf{q})\psi^*_{s'}(\mathbf{k})\psi^*_{\tilde{s}'}(\tilde{\mathbf{k}})\delta_{\tilde{\ell}_c\ell'_c}\delta_{\tilde{\ell}_v\tilde{\ell}'_v}\delta_{\ell_c\tilde{\ell}'_c}\delta_{\ell_v\ell'_v}\delta_{\mathbf{q},\mathbf{k}-\tilde{\mathbf{k}}}, \tag{22}$$

where A is the area of the sample. The above equation gives

$$g_{\mathrm{X}} = A\Delta_\sigma. \tag{23}$$

We note that the direct interaction vanishes since we let the total momentum of the exciton $Q = 0$. Here, $\mathbf{q}$ is the transferred momentum between excitons, with excitonic wavefunction being expressed in s-index notation as $\psi_{s\sigma}(\mathbf{k}) = \psi^{\ell_c\ell_v}_\sigma(\mathbf{k})$, and the factor $f^{\ell}_{s\sigma}(\mathbf{k},\mathbf{q}) = \delta_{\ell_c\ell}\psi_{s\sigma}(\mathbf{k}-\mathbf{q}) - \delta_{\ell_v\ell}\psi_{s\sigma}(\mathbf{k})$. Using the wavefunction and $t = 12$ meV, we find that the non-linearity is $g_{\mathrm{X}} \approx 0.29$ μeV μm^2. Interlayer hybridization only leads to a difference within 0.01 μeV μm^2.

Furthermore, the exciton-exciton interaction leads to a weak the non-linear blueshift which is not sufficient to account for the non-linear shift in the experiment, particularly the redshift in AFM phase. Even though this result is from a bilayer system, we do not expect our conclusions to change significantly in a system with large number of layers (bulk). Therefore, we consider additional contribution to non-linear energy shift from the coupling with magnon.

Magnon In this subsection, we investigate the non-linear energy shift due to exciton-magnon coupling. From Eq. S(12), the magnetic spin couple to the exciton through the bandgap term $\varepsilon_g(\theta_1 - \theta_2)$. In experiment, an out-of-plane magnetic field is applied to the sample (see Fig. S6). This points the spin at the equilibrium directions defined by θ_{1*} and θ_{2*}.

To obtain this equilibrium angles, we model the CrSBr as a bilayer spin system with energy density energy density (energy per unit cell) as

$$E_M = \frac{1}{N_s}\Big[\sum_{i=1}^{N_s} J\mathbf{S}^l_i \cdot \mathbf{S}^u_i - \sum_{i=1}^{N_s}\mu_0(\mathbf{S}^l_i + \mathbf{S}^u_i)\cdot\mathbf{B}\Big] \tag{24}$$

$$-\frac{1}{N_s}\sum_{i=1}^{N_s}\Big(A_x S^l_{ix}S^l_{ix} + A_x S^u_{ix}S^u_{ix}\Big) - \frac{1}{N_s}\sum_{i=1}^{N_s}\Big(A_z S^l_{iz}S^l_{iz} + A_z S^u_{iz}S^u_{iz}\Big)\Big] \tag{25}$$

where $\mathbf{S}^{l,u}_i$ is the spin for lower and upper layer. The total number of unit cell is N_s. The interlayer magnetic exchange coupling $J = 24.8$ μeV and the anistropic exchange to the easy axis is $A_x = 72.5\mu$eV and to the out-of-plane axis is $A_z = 14.4$ μeV,[37] where we set the hard axis anisotropic exchanged be zero. The last term is the magnetic anisotropy that gives the preferential direction of the spin in x-direction (we remind that CrSBr is a quasi-1D system). Here, we note that the interlayer exchange interaction J has a similar strength as the anisotropy A_x. As a function of orientation angles the energy can be written as

$$\begin{aligned} E_M(\theta_1,\theta_2) =& JS^2\cos(\theta_1-\theta_2) - \mu_0 SB(\cos\theta_1 + \cos\theta_2) \\ &- A_x S^2(\sin^2\theta_1 + \sin^2\theta_2) - A_z S^2(\cos^2\theta_1 + \cos^2\theta_2), \end{aligned} \tag{26}$$

where $S = 3/2$ is the spin at chromium site. The angle between the upper (lower) layer spin and the magnetic field is defined as θ_1 (θ_2).

To find the tilted angle with the applied magnetic field B, we minimize the total energy by solving

$$\left.\frac{\partial E_M}{\partial \theta_1}\right|_{\theta_{1*},\theta_{2*}} = 0, \quad \left.\frac{\partial E_M}{\partial \theta_2}\right|_{\theta_{1*},\theta_{2*}} = 0. \tag{27}$$

Assuming that $\theta_1 = \vartheta_{1*}$ and $\theta_2 = \theta_{2*}$ admit minimum solution of E_M, this leads to

$$\frac{\partial E_M}{\partial \theta_1} = - JS^2 \sin(\theta_{1*} - \theta_{2*}) + \mu_0 SB \sin\theta_{1*} - (A_x - A_z)S^2 \sin 2\theta_{1*} = 0, \tag{28}$$

$$\frac{\partial E_M}{\partial \theta_2} = JS^2 \sin(\theta_{1*} - \theta_{2*}) + \mu_0 SB \sin\theta_{2*} - (A_x - A_z)S^2 \sin 2\theta_{2*} = 0. \tag{29}$$

Solving the above equations, we obtain the solution that minimizes E_M. The saturation field $B_{\rm sat}$ can be obtained using Eqs. (28) and (29),

$$B = \frac{2JS\sin(\theta_{1*} - \theta_{2*}) + (A_x - A_z)S(\sin 2\theta_{1*} - \sin 2\theta_{2*})}{\mu_0(\sin\theta_{1*} - \sin\theta_{2*})} \tag{30}$$

by taking the limits $\theta_1, \theta_2 \to 0$. This gives the saturation magnetic field

$$B_{\rm sat} = 2S\frac{(J + A_x - A_z)}{\mu_0} \tag{31}$$

in the ferromagnetic phase.

The spins in CrSBr are dynamic and can fluctuate around the equilibrium directions with small angle δ_1 and δ_2 (see Figure S6). We expand the energy in the vicinity of this point as

$$E_M(\theta_{1*} + \delta_1, \theta_{2*} + \delta_2) \approx E_M(\theta_{1*}, \theta_{2*}) + a\delta_1^2 + 2b\delta_1\delta_2 + c\delta_2^2, \tag{32}$$

where

$$\begin{aligned}
a =& \frac{\partial^2 E_M(\theta_{1*}, \theta_{2*})}{\partial \theta_{*1}^2} = -JS^2\cos(\theta_{1*} - \theta_{2*}) + \mu_0 SB\cos\theta_{1*} - 2(A_x - A_z)S^2\cos 2\theta_{1*}, \\
b =& \frac{\partial^2 E_M(\theta_{1*}, \theta_{2*})}{\partial \theta_{*1}\partial\theta_{*2}} = JS^2\cos(\theta_{1*} - \theta_{2*}), \\
c =& \frac{\partial^2 E_M(\theta_{1*}, \theta_{2*})}{\partial \theta_{*2}^2} = -JS^2\cos(\theta_{1*} - \theta_{2*}) + \mu_0 SB\cos\theta_{2*} - 2(A_x - A_z)S^2\cos 2\theta_{2*}.
\end{aligned}$$

We write Eq. (32) in to the magnon normal modes as

$$E_M(\theta_{1*} + \delta_1, \theta_{2*} + \delta_2) \approx E_M(\theta_{1*}, \theta_{2*}) + \omega_-\eta_-^2 + \omega_+\eta_+^2, \tag{33}$$

where the normal mode frequencies ω_+ and ω_- are the eigenvalue of the matrix,

$$\omega_\pm = \frac{(a + c) \pm \sqrt{(a - c)^2 + 4b^2}}{2}, \tag{34}$$

and the normal eigenmodes are

$$\eta_\pm = \frac{(\omega_\pm - c)}{\sqrt{b^2 + (\omega_\pm - c)^2}}\delta_1 + \frac{b}{\sqrt{b^2 + (\omega_\pm - c)^2}}\delta_2. \tag{35}$$

Therefore, the change of the bandgap as

$$\varepsilon_g(\theta_{1*}+\delta_1,\theta_{2*}+\delta_2) =\varepsilon_0 - t\Big[\cos^2\frac{1}{2}\theta_* - \sin\theta_*(\beta_+\eta_+ - \beta_-\eta_-) - \cos\theta_*(\beta_+\eta_+ - \beta_-\eta_-)^2\Big] \tag{36}$$

with

$$\beta_+ = \frac{(1+(\omega_- - c)/b)\alpha_+}{\omega_+ - \omega_-}, \quad \beta_- = \frac{(1+(\omega_+ - c)/b)\alpha_-}{\omega_+ - \omega_-} \tag{37}$$

The magnon-exciton coupling is zero at AFM ($\theta_{1*} = -\theta_{2*} = \pi/2$) and FM ($\theta_{1*} = \theta_{2*} = 0$) phase. This implies there is no redshift in this phase if we disregard the fluctuation of the quadratic terms.

Thermal effect and incoherent magnon In nonzero finite temperature, we measure the average exciton energy in Eq. (12) due to the thermal fluctuation of the spins.[1]

$$\bar{E}_X(\theta_{1*},\theta_{2*}) =\bar{\varepsilon}_g(\theta_{1*}-\theta_{2*}) + E_b + \rho_{\mathrm{X}} g_{\mathrm{X}}, \tag{38}$$

where the average is

$$\bar{\varepsilon}_g(\theta_{1*}-\theta_{2*}) =\varepsilon_0 - t\Big[\cos^2\frac{1}{2}\theta_* - \sin\theta_*(\beta_+\langle\eta_+\rangle - \beta_-\langle\eta_-\rangle) - \cos\theta_*(\beta_+^2\langle\eta_+^2\rangle - 2\beta_+\beta_-\langle\eta_+\eta_-\rangle + \beta_-^2\langle\eta_+^2\rangle)\Big]. \tag{39}$$

The small fluctuation around θ_*, denoted as $\eta_\pm$, can take positive and negative. Therefore, we may expect $\langle\eta_\pm\rangle = 0$ and disregard the linear coupling term (second term). However, in the last term, we expect $\langle\eta_\pm^2\rangle \propto n_\pm$ where $n_\pm$ is the total number of the ($\pm$) magnons modes in the sample. $\eta_\pm^2$ is proportional to the amplitude square. For the the cross-term, we have $\langle\eta_+\eta_-\rangle = \langle\eta_+\rangle\langle\eta_-\rangle = 0$, since η_+ and η_- are two independent orthogonal modes. This reduces the measure bandgap to

$$\bar{\varepsilon}_g(\theta_{1*},\theta_{2*}) =\varepsilon_0 - t\Big[\cos^2\frac{1}{2}\theta_* - \cos\theta_*(\beta_+^2\langle\eta_+^2\rangle + \beta_-^2\langle\eta_+^2\rangle)\Big] \tag{40}$$

To calculate the $\langle\eta_\pm\rangle$, we model the thermal effects using canonical ensemble with the partition function as

$$Z = \int_{-\eta_+^c}^{\eta_+^c} d\eta_+ \int_{-\eta_-^c}^{\eta_-^c} d\eta_- \mathrm{e}^{-\frac{1}{k_BT}[E_M(\theta_{1*},\theta_{2*}) + \omega_-\eta_-^2 + \omega_+\eta_+^2]} = \mathrm{e}^{-\frac{1}{k_BT}E_M(\theta_{1*},\theta_{2*})} \prod_{i=\pm}\sqrt{\frac{\pi k_BT}{\omega_i}}\mathrm{erf}\Big(\eta_i^c\sqrt{\frac{\omega_i}{k_BT}}\Big), \tag{41}$$

where $\eta_\pm^c$ is the cutoff that are related to the maximum fluctuation in δ_1 and δ_2. Therefore, this gives

$$\begin{aligned}\langle\eta_\pm^2\rangle =&\frac{1}{Z}\int_{-\eta_+^c}^{\eta_+^c} d\eta_+ \int_{-\eta_-^c}^{\eta_-^c} d\eta_- \eta_\pm^2 \mathrm{e}^{-\frac{1}{k_BT}[E_M(\theta_{1*},\theta_{2*}) + \omega_-\eta_-^2 + \omega_+\eta_+^2]} \\ =&\Big(\frac{k_BT}{2\omega_\pm}\mathrm{erf}(\eta_\pm^c\sqrt{\frac{\omega_\pm}{k_BT}}) - \frac{\eta_\pm^c}{\sqrt{\pi}}\mathrm{e}^{-\frac{(\eta_\pm^c)^2}{k_BT}}\Big)/\mathrm{erf}(\eta_\pm^c\sqrt{\frac{\omega_\pm}{k_BT}})\end{aligned} \tag{42}$$

In the low-temperature $\omega_\pm/k_BT \to \infty$. This gives the following simple result,

$$\langle\eta_\pm^2\rangle = \frac{1}{2}k_BT/\omega_\pm. \tag{43}$$

Here, the temperature T is the magnonic temperature which is proportional to the pump intensity. This result can also be understood intuitively by considering the total number of thermally-excited magnon, since the k_BT is the thermal energy and $\omega_\pm$ is a single magnon energy.

Note that he result in Eq. (43) holds only for the case of magnon energy being sufficiently large. However, for the cases where the magnon energy is small we can no longer take $\omega_\pm/k_BT \to \infty$. In the case we take a limit $\omega_\pm \to 0$ in Eq.(42), leading to

$$\langle \eta_\pm^2 \rangle \approx \frac{(\eta_\pm^c)^2}{3}. \tag{44}$$

In this case, almost every available low-energy magnons get excited.

Therefore, we arrive at the exciton energy written as

$$\bar{E}_X(\theta_{1*},\theta_{2*}) = \varepsilon_0 - t\Big[\cos^2\frac{1}{2}(\theta_{1*}-\theta_{2*}) - \Big(\beta_+^2\langle\eta_+^2\rangle + \beta_-^2\langle\eta_-^2\rangle\Big)\cos(\theta_{1*}-\theta_{2*})\Big] + E_b + \rho_{\mathrm{X}} g_{\mathrm{X}} \tag{45}$$

where $\varepsilon_g(\theta_{1*}-\theta_{2*})$ is the bandgap, E_b is the exciton binding energy, and g_{X} is the exciton-exciton exchange interacting strength. Using Eqs. (34), (35), and (37), we obtain the important result for explaining the findings in different magnetic configurations:

$$\bar{E}_X(\pi/2,-\pi/2) = \varepsilon_0 - t\frac{k_BT}{\omega_-} + E_b + \rho_{\mathrm{X}} g_{\mathrm{X}}, \qquad \text{(AFM)} \tag{46}$$

$$\bar{E}_X(0,0) = \varepsilon_0 - t + t\frac{2}{3}(\eta_-^c)^2 + E_b + \rho_{\mathrm{X}} g_{\mathrm{X}}, \qquad \text{(FM)} \tag{47}$$

where in the FM phase the magnon energy near $B = B_{\mathrm{sat}}$ is very small. As $B > B_{\mathrm{sat}}$, the incoherent magnon (η_--mode) shift in FM phase take the general form in Eq. S(42).

To investigate the polaritonic response in CrSBr, we recognize that the created exciton is hybridized with the intrinsic cavity mode forming a self-hybridize polariton in strong light-matter coupling regime. We model this self-hybridized polariton as follows:

$$\mathcal{H}_p = \begin{bmatrix} \omega_c & \Omega \\ \Omega & \bar{E}_X(\theta_{1*},\theta_{2*}) \end{bmatrix}, \tag{48}$$

where ω_c is the intrinsic cavity mode with $\omega_c \approx \varepsilon_0 + E_b$. The Rabi splitting Ω also experiences a non-linear response due to phase space filling effect.[38] The lower polariton in this system has the energy

$$\mathcal{E} = \frac{1}{2}[\omega_c + E_X(\theta_{1*},\theta_{2*})] - \sqrt{\frac{1}{2}[\omega_c - E_X(\theta_{1*},\theta_{2*})]^2 + \Omega^2} \tag{49}$$

In the above, we may approximate the Rabi splitting as $\Omega = \Omega_0\left(1 - \frac{1}{2}\frac{a_X^2\rho_{\mathrm{X}}}{(1+\gamma_c)(1+\gamma_v)}\right)$,[38] where $\gamma_{c/v} = m_{c/v}/(m_c + m_v)(a_X/\sqrt{A})$ with $m_{c/v} = \sqrt{m_{c/v,x}m_{c/v,y}}$ being the geometrical average of the conduction/valence band masses and $a_X = \langle r\rangle$ being the average distance of the between the electron and the hole (exciton size) from theoretical estimation is

$$a_X = \begin{cases} 1.0\text{nm} & \text{AFM, intralayer exciton,} \\ 1.1\text{nm} & \text{FM, hybridized exciton.} \end{cases} \tag{50}$$

Also, the Rabi splitting in low-density regime is $\Omega_0 \approx 0.24$ eV.[1] We write the energy shift due to the small change in temperature ΔT and exciton density $\Delta\rho_{\mathrm{X}}$ by expanding it as

$$\Delta\mathcal{E} = \mathcal{B}\Delta T + \mathcal{A}\Delta\rho_{\mathrm{X}}, \tag{51}$$

where

$$\mathcal{B} = \Big[\frac{1}{2} + \frac{\omega_c - \bar{E}_X^{(0)}}{2\Lambda}\Big]\frac{\partial \bar{E}_X}{\partial T}, \tag{52}$$

$$\mathcal{A} = \Big(\frac{1}{2} + \frac{\omega_c - \bar{E}_X^{(0)}}{2\Lambda}\Big)\frac{\partial \bar{E}_X}{\partial \rho_{\mathrm{X}}} - \frac{\Omega_0}{2\Lambda}\frac{\partial \Omega}{\partial \rho_{\mathrm{X}}}. \tag{53}$$

Here, we have defined $\Lambda = \sqrt{\frac{1}{2}(\omega_c - E_X^{(0)})^2 + \Omega_0^2}$ with $E_X^{(0)} = \varepsilon_0 - t\cos^2\frac{1}{2}(\theta_{1*} - \theta_{2*}) + E_b$. The derivatives are

$$\frac{\partial \bar{E}_X}{\partial T} = \Big(\beta_+^2\frac{\partial\langle\eta_+^2\rangle}{\partial T} + \beta_-^2\frac{\partial\langle\eta_-^2\rangle}{\partial T}\Big)\cos\tfrac{1}{2}(\theta_{1*} - \theta_{2*}), \tag{54}$$

$$\frac{\partial \bar{E}_X}{\partial \rho_{\mathrm{X}}} = g_{\mathrm{X}}, \tag{55}$$

$$\frac{\partial \Omega}{\partial \rho_{\mathrm{X}}} = -\frac{\Omega_0 a_X^2/2}{(1+\gamma_c^2)(1+\gamma_v^2)}. \tag{56}$$

Assuming $\gamma_{c,v} \approx 0$, we find the saturation factor $\frac{\partial\Omega}{\partial\rho_{\mathrm{X}}} \approx -0.24\ \mu\mathrm{eV}\mu\mathrm{m}^2$ which is as large as g_{X} and it is another important nonlinear effect. The energy shift due to laser power is

$$\Delta\mathcal{E}_{\mathrm{AFM}} = -\Big[\frac{1}{2} + \frac{\omega_c - \bar{E}_X^{(0)}}{2\Lambda}\Big]\frac{tk_B}{\omega_-}\Delta T + \Big[\Big(\frac{1}{2} + \frac{\omega_c - \bar{E}_X^{(0)}}{2\Lambda}\Big)g_{\mathrm{X}} + \frac{\Omega_0}{2\Lambda}\frac{a_X^2/2}{(1+\gamma_c^2)(1+\gamma_v^2)}\Big]\Delta\rho_{\mathrm{X}}, \quad \text{(AFM)} \tag{57}$$

$$\Delta\mathcal{E}_{\mathrm{FM}} = \Big[\Big(\frac{1}{2} + \frac{\omega_c - \bar{E}_X^{(0)}}{2\Lambda}\Big)g_{\mathrm{X}} + \frac{\Omega_0}{2\Lambda}\frac{a_X^2/2}{(1+\gamma_c^2)(1+\gamma_v^2)}\Big]\Delta\rho_{\mathrm{X}}, \quad \text{(FM)} \tag{58}$$

where the magnon energy $\omega_- = S^2(J + A_x - A_z)$ with the magnetic exchange couplings $J = 24.8\ \mu$eV, $A_x = 72.5\ \mu$eV and $A_z = 14.4\ \mu$eV.[37]

In the FM phase, since the magnon energy is very small, almost all the available magnonic excited states are depleted immediately with small temperature change. This results in the very low temperature-dependent blueshift. Therefore, in this case, the exciton energy nonlinear blueshift is mostly coming from the exciton-exciton exchange interaction. This is consistent to the non-linear response that we observed in high-power measurement. We found the maximum blue shift (Fig. 2h) is $\Delta\mathcal{E} = 2.3$ meV.

As we can see, the magnon fluctuating term in AFM phase is negative leading to the redshift. Moreover, we find this effect rather strong. Changing the temperature by $\Delta T \approx 1.6$ K is sufficient to generate a $\Delta\mathcal{E}_{\mathrm{FM}} = -2$ meV redshift in exciton energy if we assume the maximum blueshift coming from the saturation and exciton-exciton interaction is $\Delta\mathcal{E}_{\mathrm{FM}} = 2.3$ meV. Furthermore, we have let $\omega_c - E_X^{(0)} \approx 0$ (small detuning). Therefore, it is very likely the blueshift coming from exciton-exciton interaction is compensated, leading to the overall redshift.

Supplementary note 6: Correlation measurements of the polariton condensates in FM order

Figure S8a shows a schematics of the Michelson interferometer for measuring the first-order correlation of polariton condensate. As an example, the cartoon of mesa is used to demonstrate the spatial inversion of the images reflected from two arms. In our measurements, the reflected beam from the reference arm is aligned to transmit through the center of the last focusing lens. The reflected beam from the delay arm is parallel to that of the reference arm, but has a spatial displacement. Both images are focused and overlapped on the detector. More detailed operations of this interferometer can be found in the Methods section of the manuscript.

Figure S8b shows the power dependent interference pattern (upper panels) as well as the calculated first-order correlation function (lower panels) of the LPB in FM order of sample position 2 (cavity detuning voltage of 38 V and external magnetic field of 3 T). Its PL spectrum at a minimum pump power is shown in Fig. S4c. The excitation condition of the power dependence is the same as in Fig. 3a of the manuscript. We can see that the maximum interference visibility as well as the first-order correlation function $g^{(1)}(\vec{r},0)$ is obtained at an averaged pump power around 29 mW, and then both of them decrease at higher pump powers, corresponding to the same turning point of the coherence length decrease shown in Fig. 3c of the manuscript.

Figure S9 show the complete power dependent second-order correlation measurements of the LPBs in AFM and FM orders in Fig. S4c. we can see that in both magnetic orders the $g^{(2)}(0)$ decreases with increasing pump power, signifying the coherence build-up of the polaritons which is consistent with the 1st-order coherence measurements in Supplementary Fig. S8b and Fig. 3a of the manuscript. The power-dependent $g^{(2)}(0)$ values are summarized in Fig. 3c of the manuscript.

Reference

1. Dirnberger, F. *et al.* Magneto-optics in a van der waals magnet tuned by self-hybridized polaritons. *Nature* **620**, 533–537 (2023).
2. Wang, T. *et al.* Magnetically-dressed crsbr exciton-polaritons in ultrastrong coupling regime. *Nature Communications* **14**, 5966 (2023).
3. Meineke, C. *et al.* Ultrafast exciton dynamics in the atomically thin van der waals magnet crsbr. *Nano Letters* **24**, 4101–4107 (2024).
4. Rizzo, D. J. *et al.* Visualizing atomically layered magnetism in crsbr. *Advanced Materials* **34**, 2201000 (2022).
5. Tschudin, M. A. *et al.* Imaging nanomagnetism and magnetic phase transitions in atomically thin crsbr. *Nature Communications* **15**, 6005 (2024).
6. Chernikov, A., Ruppert, C., Hill, H. M., Rigosi, A. F. & Heinz, T. F. Population inversion and giant bandgap renormalization in atomically thin ws2 layers. *Nature Photonics* **9**, 466–470 (2015).
7. Wang, G. *et al.* Colloquium: Excitons in atomically thin transition metal dichalcogenides. *Reviews of Modern Physics* **90**, 021001 (2018).
8. Kappei, L., Szczytko, J., Morier-Genoud, F. & Deveaud, B. Direct observation of the mott transition in an optically excited semiconductor quantum well. *Physical review letters* **94**, 147403 (2005).
9. Huber, R., Kaindl, R. A., Schmid, B. A. & Chemla, D. S. Broadband terahertz study of excitonic resonances in the high-density regime in gaas/ al x ga 1- x as quantum wells. *Physical Review B—Condensed Matter and Materials Physics* **72**, 161314 (2005).
10. Rossbach, G. *et al.* High-temperature mott transition in wide-band-gap semiconductor quantum wells. *Physical Review B* **90**, 201308 (2014).
11. Cain, N. *et al.* Photoluminescence of cdte/cdmnte multiple quantum wells excited near the mott transition. *Journal of luminescence* **75**, 269–275 (1997).
12. Teran, F., Chen, Y., Potemski, M., Wojtowicz, T. & Karczewski, G. Optical properties of cd 1- x mn x te quantum wells across the mott transition: An interband spectroscopy study. *Physical Review B—Condensed Matter and Materials Physics* **73**, 115336 (2006).
13. Klein, J. *et al.* The bulk van der waals layered magnet crsbr is a quasi-1d material. *ACS Nano* **17**, 5316–5328 (2023).

14. Ziebel, M. E. *et al.* Crsbr: an air-stable, two-dimensional magnetic semiconductor. *Nano Letters* **24**, 4319–4329 (2024).

15. Wu, F. *et al.* Quasi-1d electronic transport in a 2d magnetic semiconductor. *Advanced Materials* **34**, 2109759 (2022).

16. Smolenski, S. *et al.* Large exciton binding energy in the bulk van der waals magnet crsbr. *arXiv preprint arXiv:2403.13897* (2024).

17. Semina, M. *et al.* Excitons and trions in crsbr bilayers. *arXiv preprint arXiv:2411.15493* (2024).

18. Liu, W. *et al.* A three-stage magnetic phase transition revealed in ultrahigh-quality van der waals bulk magnet crsbr. *ACS nano* **16**, 15917–15926 (2022).

19. Scholes, G. D. Insights into excitons confined to nanoscale systems: electron–hole interaction, binding energy, and photodissociation. *ACS nano* **2**, 523–537 (2008).

20. Nguyen, D.-T. *et al.* Excitonic nonlinearities in single-wall carbon nanotubes. *physica status solidi (b)* **249**, 907–913 (2012).

21. Nguyen, D. *et al.* Excitonic homogeneous broadening in single-wall carbon nanotubes. *Chemical Physics* **413**, 102–111 (2013).

22. Wang, F., Dukovic, G., Brus, L. E. & Heinz, T. F. The optical resonances in carbon nanotubes arise from excitons. *Science* **308**, 838–841 (2005).

23. Lauret, J. *et al.* Optical transitions in single-wall boron nitride nanotubes. *Physical review letters* **94**, 037405 (2005).

24. Wirtz, L., Marini, A. & Rubio, A. Excitons in boron nitride nanotubes: dimensionality effects. *Physical review letters* **96**, 126104 (2006).

25. Cassabois, G., Valvin, P. & Gil, B. Hexagonal boron nitride is an indirect bandgap semiconductor. *Nature photonics* **10**, 262–266 (2016).

26. Kavokin, A., Baumberg, J. J., Malpuech, G. & Laussy, F. P. *Microcavities* (Oxford university press, 2017).

27. Klingshirn, C. F. *Semiconductor Optics* (Springer Science & Business Media, 2012).

28. Mott, N. F. The basis of the electron theory of metals, with special reference to the transition metals. *Proceedings of the Physical Society. Section A* **62**, 416 (1949).

29. Mott, N. *Metal-insulator transitions* (CRC Press, 2004).

30. Ceferino, A., Song, K. W., Magorrian, S. J., Zólyomi, V. & Fal'ko, V. I. Crossover from weakly indirect to direct excitons in atomically thin films of inse. *Physical Review B* **101**, 245432 (2020).

31. Danovich, M. *et al.* Localized interlayer complexes in heterobilayer transition metal dichalcogenides. *Physical Review B* **97**, 195452 (2018).

32. López-Paz, S. A. *et al.* Dynamic magnetic crossover at the origin of the hidden-order in van der waals antiferromagnet crsbr. *Nature Communications* **13** (2022).

33. Keldysh, L. V. Coulomb interaction in thin semiconductor and semimetal films. *Soviet Journal of Experimental and Theoretical Physics Letters* **29**, 658 (1979).

34. Rytova, N. The screened potential of a point charge in a thin film. *Moscow University Physics Bulletin* **3**, 18 (1967).

35. Cudazzo, P., Tokatly, I. V. & Rubio, A. Dielectric screening in two-dimensional insulators: Implications for excitonic and impurity states in graphane. *Physical Review B* **84**, 085406 (2011).

36. Song, K. W. & Kyriienko, O. Electrically tunable and enhanced nonlinearity of moiré exciton-polaritons in transition metal dichalcogenide bilayers. *arXiv e-prints* arXiv:2406.08263 (2024).

37. Wang, Y., Luo, N., Zeng, J., Tang, L.-M. & Chen, K.-Q. Magnetic anisotropy and electric field induced magnetic phase transition in the van der waals antiferromagnet crsbr. *Physical Review B* **108**, 054401 (2023).

38. Song, K. W., Chiavazzo, S. & Kyriienko, O. Microscopic theory of nonlinear phase space filling in polaritonic lattices. *Physical Review Research* **6**, 023033 (2024).

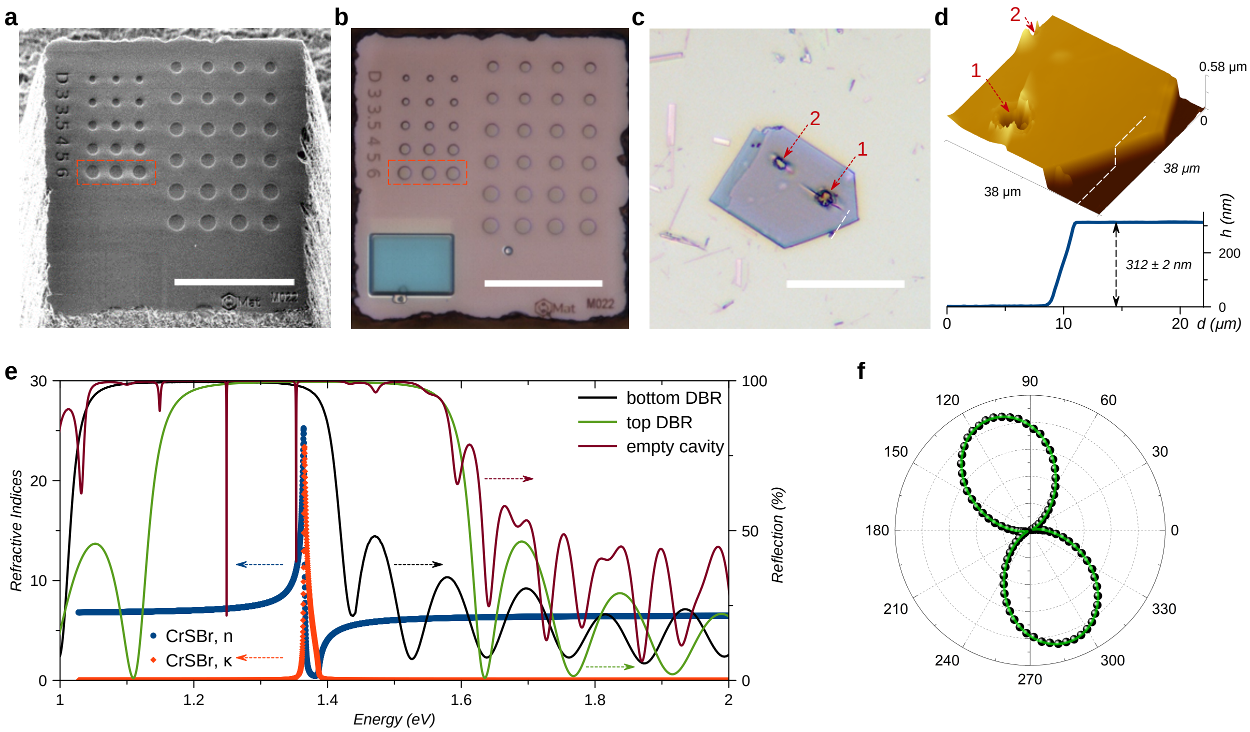

Supplementary Fig. S1| Cavity and material properties. a. Scanning electron microscope image of the mesa after FIB etching. The 6 μm lens pits are marked by the red frame. **b.** Optical microscope of the mesa after sputtering with DBR. The 6 μm lenses (concave DBR) are marked by the red frame. **c.** Microscope image of the CrSBr flake transferred on the bottom DBR. The scale bars in **a-c** are all 50 μm. The holes (1: 6 μm$\times$ 4 μm; 2: 4 μm $\times$ 5 μm) are burned through the 6 μm lenses by 725 nm femtosecond laser with high power (0.92 nJ/pulse). **d.** Upper panel: atomic force microscopy of the CrSBr flake in **c**. Lower panel: step profile along the white dashed lines in the upper panel and **c**. The measured thickness (h=312$\pm$2 nm) matches perfectly with the simulation by the transfer matrix in Fig. 1c of the manuscript. **e.** Reflection of the top and bottom DBR, and empty cavity with a gap of 4025 nm, simulated by the transfer matrix method, and the complex refractive index $\tilde{n} = n + i\kappa$ of CrSBr used for the transfer matrix simulation in Fig. 1c of the manuscript. **f.** Polarization dependent PL emission intensity (black dots) of the LPB at 20 V detuning voltage in Fig. 1d of the manuscript. The fit (green) determines the crystallographic b-axis as 110° or 290° in our experimental geometry.

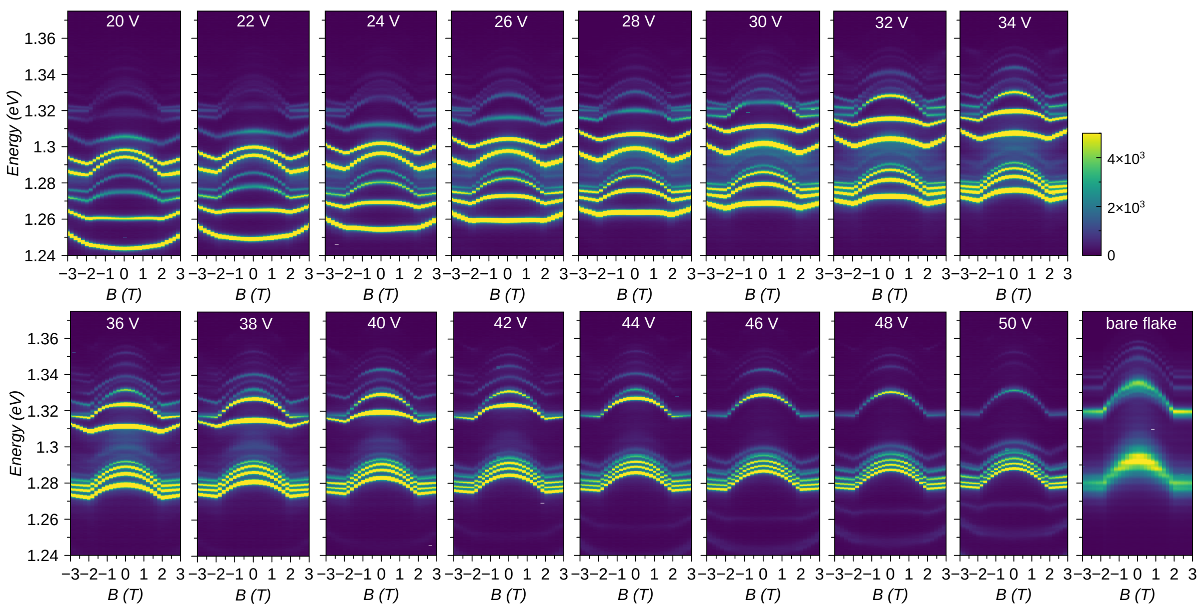

Supplementary Fig. S2| Magneto-PL of sample position 1 at different cavity detunings. The measurements are performed between ± 3 T for detuning DC voltages from 20 V to 50 V. All graphs share the same colorbar. The cavity length gets smaller and the modes blueshift for saturation magnetic fields $|B| \geq 2$ T. The drifts for magnetic field intensity $|B| < 2$ T is less than 1 meV.

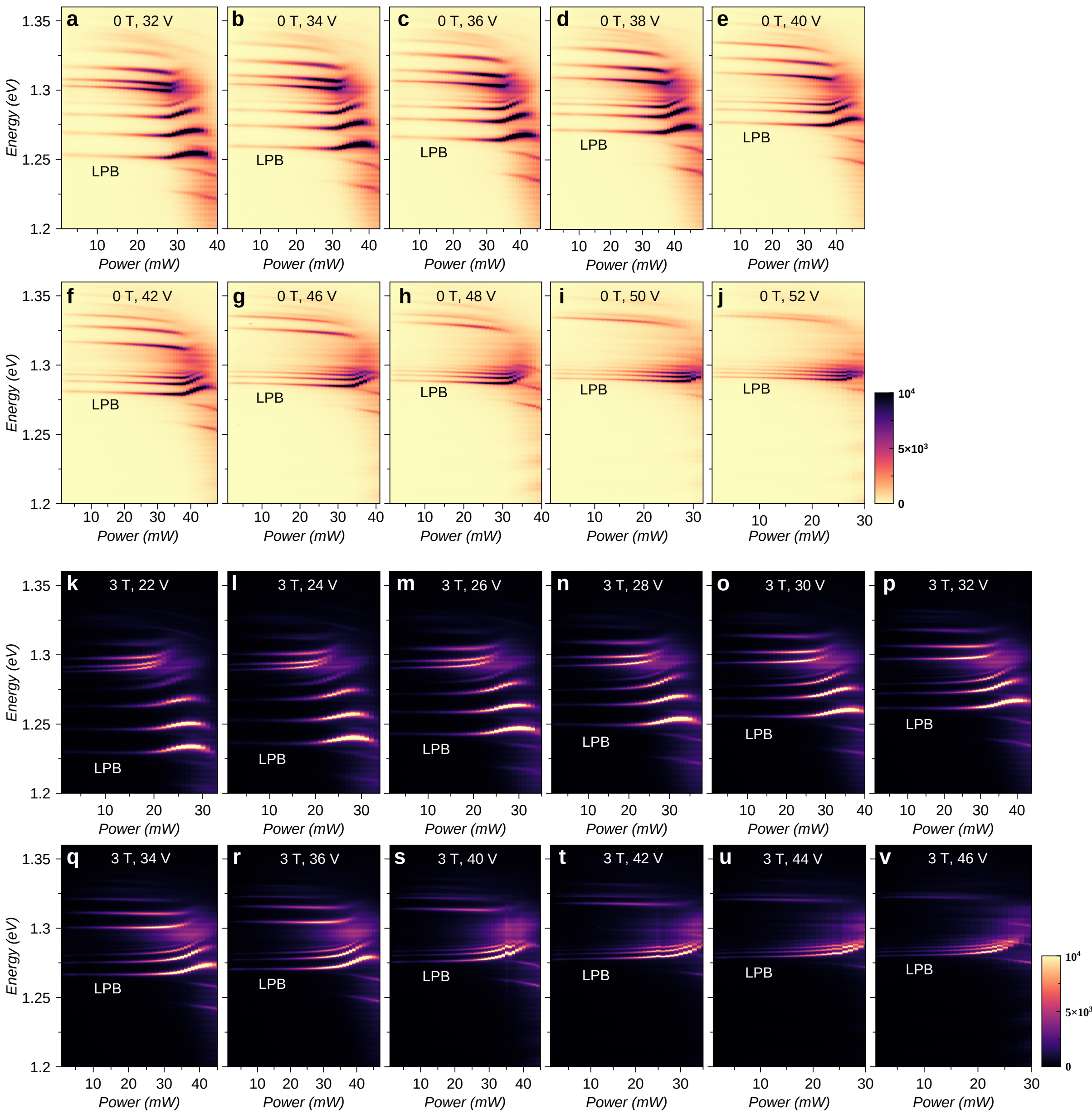

Supplementary Fig. S3| Pump power dependent PL measurements of sample position 2. a-j. cavity detuning voltages of 32-52 V and AFM order (0 T). **k-v.** cavity detuning voltages of 22-46 V and FM order (3 T). The two colorbars apply to measurements with different magnetic orders. The voltages in **a-j** and **k-v** correspond to those in cavity detuning PL measurements in Fig. S4a and Fig. S4b, respectively. The power dependent PL measurements at 44 V (0 T) and 38 V (3 T) detuning voltages are shown in Fig. 2a and Fig. 2b in the manuscript, respectively.

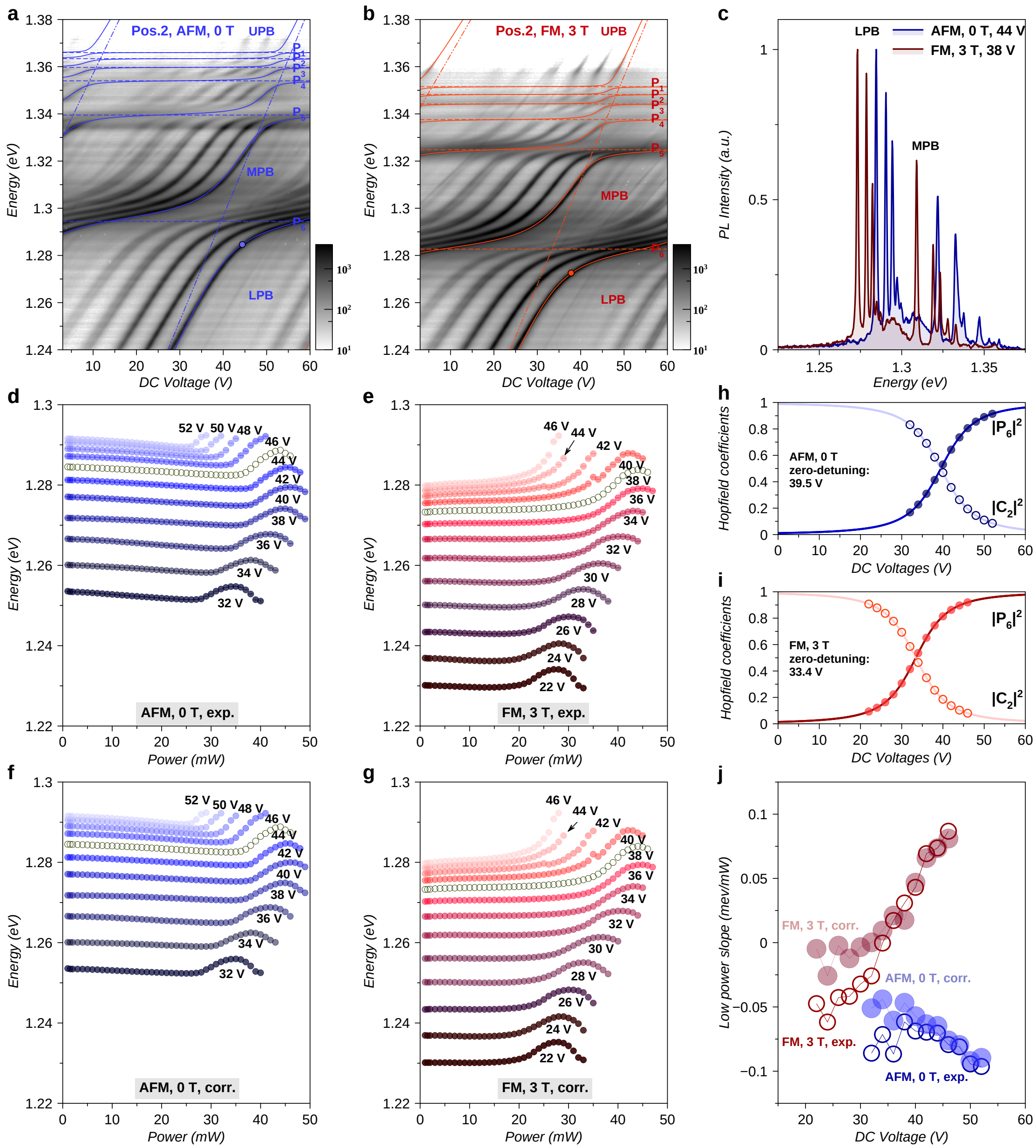

Supplementary Fig. S4| LPB non-linearity with different cavity detunings and magnetic orders. PL measurements of sample position 2 as a function of cavity detunings (DC voltages) in **a.** AFM order (0 T) and **b.** FM order (3 T). The experiments are performed with a pump power of 0.5 mW, far below the condensate thresholds. Additionally plotted lines are the fitting of the polariton modes (solid), self-hybridized polaritons (dashed), and the cavity modes (dotted-dashed), resulting from a 9×9 coupled oscillators model. **c.** PL spectra at detuning voltages of 44 V of the AFM order and 38 V of the FM order that are marked by the dots in **a** and **b**. These two detuning voltages correspond to the same detuning energy relative to the P_6 self-hybridized polariton, where the polariton non-linearity in Fig. 2 of the manuscript is measured. Detuning dependent LPB energy shifts with increasing pump power in **d.** AFM order (0 T) and **e.** FM order (3 T), fitted from the data in Fig. S2. Corrected LPB energy shifts with increasing pump in **f.** AFM order (0 T) and **g.** FM order (3 T). **h.** AFM order (0 T), and **i.** FM order (3 T) Hopfield coefficients (the ratios of P_6 self-hybridized polariton: $|P_6|$ and the external cavity mode: $|C_2|$) of the LPBs with different detunings, which are calculated by a 2×2 coupled oscillator model in Eqs. S8-S11. The dots and circles mark the detunings where polariton non-linearities are measured in **d-g** and Fig. S2. **j.** The experimental (empty symbols) and corrected (filled symbols) slopes of the LPB energy shifts below 20 mW in **d-g**, fitted by a linear function.

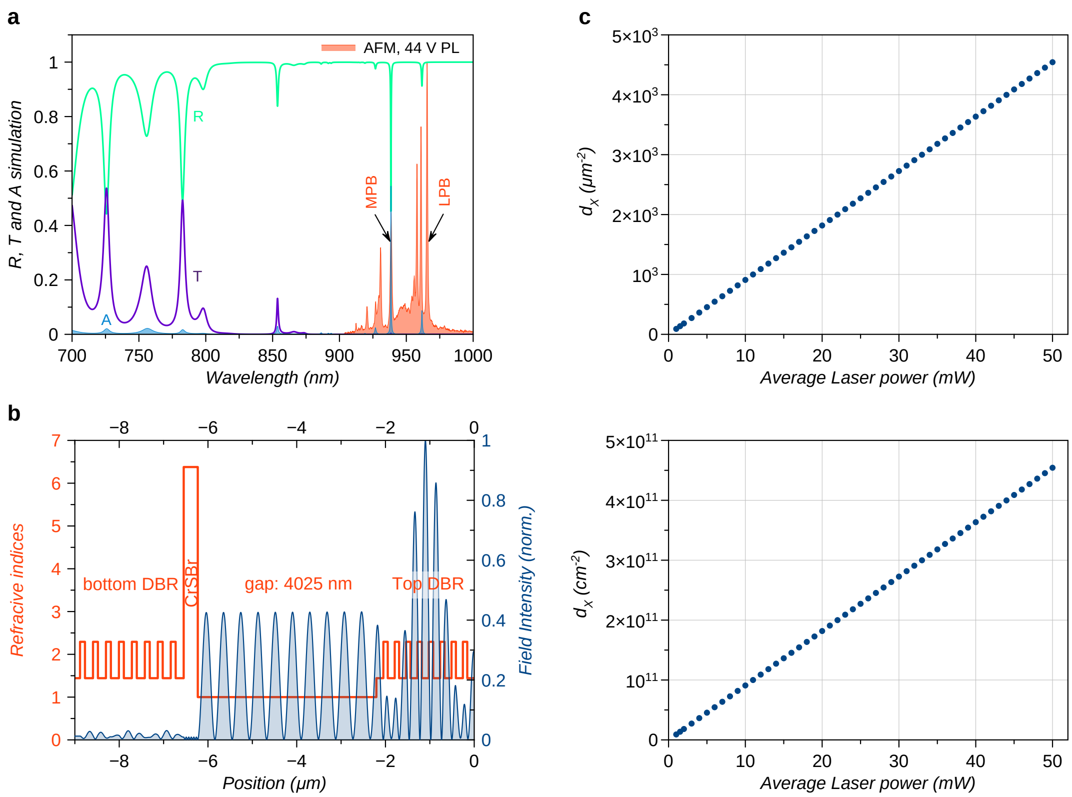

Supplementary Fig. S5| Simulation of full cavity structure. a. Simulated reflection (R), transmission (T), and absorption (A) of 965 nm light in the open cavity with a gap of 4025 nm by transfer matrix method. The PL spectrum (AFM order, 44 V) matches very well the simulations. There is a few nanometers discrepancy of the LPB, probably due to the admixture of the unknown photonic tunneling. The absorption at 725 nm is 0.0209. **b.** The electric field intensity distribution in the cavity and corresponding structure of the dielectric layers of the cavity. **c.** Conversion between exciton density in each layer and the average pump power. Top (bottom) panel: unit in μm^{-2} (cm^{-2}).

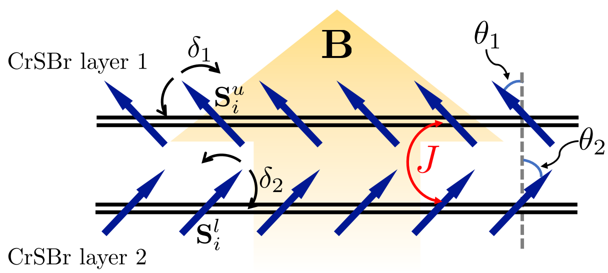

Supplementary Fig. S6| Schematic diagram for the spin model in bilayer CrSBr. The spin in the upper and lower layer at site i are $\mathbf{S}_i^u$ and $\mathbf{S}_i^l$. Their interlayer spin exchange coupling is J. In the presence of the uniform out-of-plane magnetic field $\mathbf{B}$, the spins $\mathbf{S}_i^u$ ($\mathbf{S}_i^l$) become tilted, forming an angle θ_1 (θ_2) with respect to $\mathbf{B}$-field. In non-zero temperature, the spins $\mathbf{S}_i^u$ ($\mathbf{S}_i^l$) fluctuate around its equilibrium orientation with small angle δ_1 (δ_2).

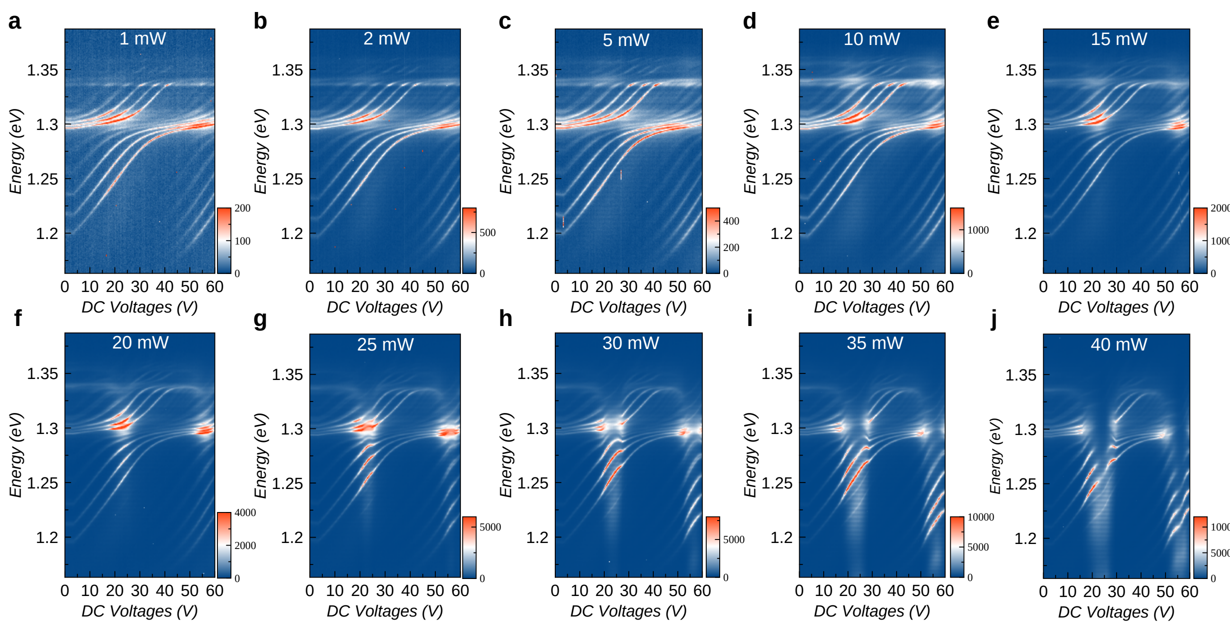

Supplementary Fig. S7| Power dependent PL of cavity detuning on sample position 2 (AFM, 0 T). The threshold phenomenon is clear around 20 mW pump power. The stimulated polaritonic scattering is then more obvious for higher powers, leading to the condensation into the lowest polariton modes (for cavity detuning around 22 V and 55 V of two consecutive longitudinal mode sets). At maximum power of 40 mW, the Rabi gap collapses and the system reaches the optical saturation.

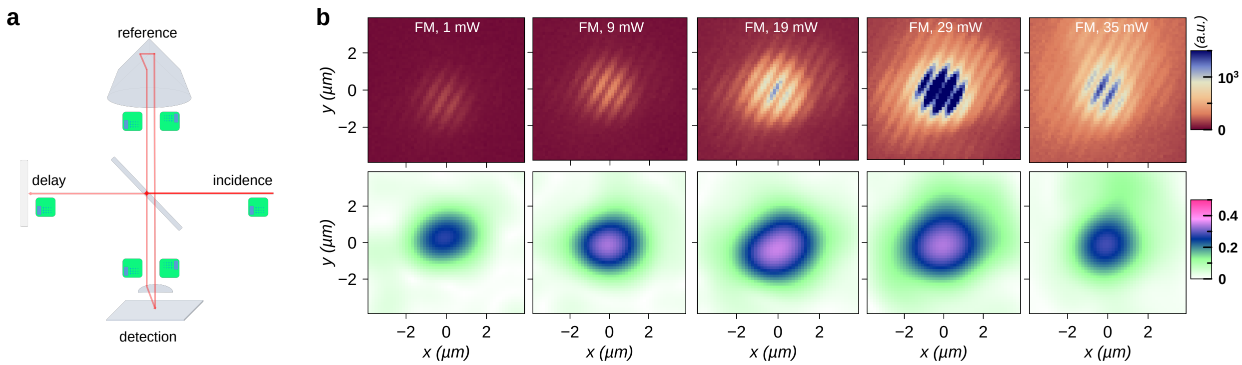

Supplementary Fig. S8| First-order correlation of the exciton-polariton condensate at 3 T. a. Schematics of the Michelson interferometer. The sample image as well as the real-space emission patterns from the reference arm is spatially inverted. **b.** Top panels: Pump power dependent zero-delay interference patterns of the FM order (3 T, 38 V detuning) LPB emission in Fig. S4c. Bottom panels: calculated spatially-resolved first-order correlation $g^{(1)}(\vec{r}, 0)$ at the pump powers corresponding to the upper panels.

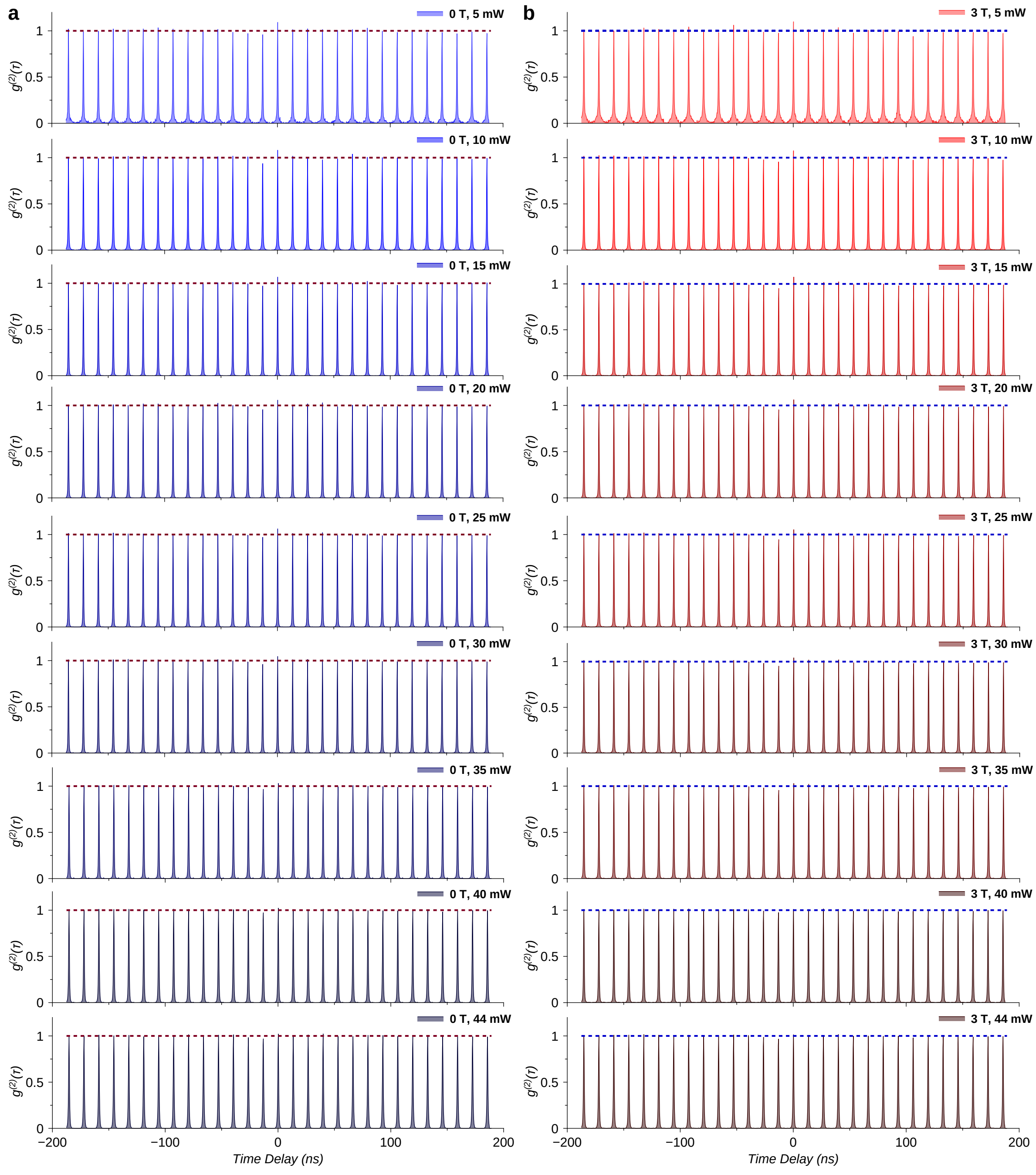

Supplementary Fig. S9| Second-order correlation of the exciton-polariton condensate. a. Pump power dependent $g^{(2)}(\tau)$ of the LPB emission in AFM order (0 T, 44 V) of Supplementary Fig. S4c. **b.** Pump power dependent $g^{(2)}(\tau)$ of the LPB emission in FM order (3 T, 38 V) of Supplementary Fig. S4c.